WP17ER-CPR(18) 20761

L Sanchis-Sanchez et al.

Main parametric dependencies of the fast-ion edge resonant transport layer induced by 3D perturbative fields in the ASDEX upgrade tokamak

Preprint of Paper to be submitted for publication in Proceeding of 45th European Physical Society Conference on Plasma Physics (EPS)

This work has been carried out within the framework of the EUROfusion Consortium and has received funding from the Euratom research and training programme 2014-2018 under grant agreement No 633053. The views and opinions expressed herein do not necessarily reflect those of the European Commission.

Main Parametric Dependencies of the Fast-Ion Edge Resonant Transport Layer Induced by 3D Perturbative Fields in the ASDEX Upgrade Tokamak

L. Sanchis[1,2], M. Garcia-Munoz[1,2], A. Snicker[3], J. Galdon-Quiroga[1,2], D. A. Ryan[4], M. Nocente[5], J. F. Rivero-Rodriguez[1,2], M. Rodriguez-Ramos[2]. L. Chen[6], W. Suttrop[7], E. Viezzer[1,2], M. Willensdorfer[7], M. A. Van Zeeland[8], D. Zarzoso[9], F. Zonca[10] the ASDEX Upgrade Team and the EUROfusion MST1 Team‡

1 Dept. of Atomic, Molecular and Nuclear Physics, University of Seville, Avda. Reina Mercedes, 41012 Seville, Spain

2 Centro Nacional de Aceleradores CNA (Universidad de Sevilla, Junta de Andalucía, CSIC), Avda. Thomas A. Edison 7, 41092 Seville, Spain

[3] *Dept. of Applied Physics, Aalto University, FI- 00076, Aalto, Finland*

[4] *CCFE, Culham Science Centre, OX14 3DB, Abingdon, UK*

[5] *Universita degli Studi di Milano-Bicocca, Piazza della Scienza 3, 20126, Milano, Italy*

[6] *IFTS, Zhejiang University, 310027, 310027, Hangzhou, China*

[7] *Max Planck Institute for Plasma Physics, Boltzmannstr. 2, 85748 Garching, Germany*

[8] *General Atomics, CA 92186-5608, San Diego, USA*

[9] *Aix-Marseille Université, CNRS, PIIM, UMR 7345, Mareseille, France*

[10] *ENEA C.R. Frascati, CP 65-00044, Frascati, Italy*

E-mail: `lsanchis@us.es`

Abstract. In recent experiments at the ASDEX Upgrade tokamak the existence of an Edge Resonant Transport Layer (ERTL) was revealed as the main transport mechanism responsible for the measured fast-ion losses in the presence of externally applied 3D fields. The Monte Carlo orbit-following code ASCOT was used to study the fast-ion transport including the plasma response calculated with MARS-F, reproducing a strong correlation of fast-ion losses with the 3D fields poloidal mode spectra. In this work, a description of the physics underlying the ERTL is presented by means of numerical simulations together with an analytical model and experimental measurements to validate the results. The degradation of fast-ion confinement is calculated in terms of the variation of the toroidal canonical momentum (δP_ϕ). This analysis reveals resonant patterns at the plasma edge activated by 3D perturbations

‡ See the author list of *Overview of progress in European Medium Sized Tokamaks towards an integrated plasma–edge/wall solution* by H. Meyer et al., Nucl. Fusion **57** 102014 2017.

and emphasising the relevance of nonlinear resonances. The impact of collisions and the radial electric field on the ERTL is analyzed.

1. Introduction

Edge Localized Modes (ELMs), present in high confinement regimes in current tokamak plasmas, must be kept under control to limit energy and particle losses, which at current levels would be unacceptable in future fusion devices such as ITER. Therefore, substantial efforts are being focused on the development of reliable techniques capable of suppressing or mitigating these instabilities in high confinement regimes. One of the leading techniques among them is the application of external magnetic perturbations (MPs) [1, 2, 3, 4]. These perturbative fields have, however, an impact on the overall plasma stability and confinement. The plasma response depends on several factors such as magnetic equilibrium, main plasma parameters and the perturbation spectrum. The mechanism responsible for the ELM mitigation has been evidenced to depend strongly on the plasma response to the applied MP [5, 6] and its poloidal mode spectra [7, 8]. Considering this, the effect of the MPs poloidal mode spectrum and of the plasma response generated by the perturbation, needs to be analysed. This effect is most pronounced on the energetic particles with relatively long slowing-down times [9] and must be carefully assessed, as they will be present in future fusion devices. Previous numerical simulations of the impact on ELM control coils on fast-ion confinement in ITER [10, 11] have predicted up to a 20% power loss for the neutral beam injection (NBI) and 6% for fusion born alpha particles. First experiments at AUG and DIII-D have shown that the externally applied perturbations can lead to a degradation of the energetic particle confinement [12, 13, 14] for certain magnetic configurations, compromising the integrity of the device.

Experiments on both ASDEX Upgrade (AUG) and DIII-D show that the poloidal mode spectra of the applied 3D resonant magnetic perturbation commonly used to mitigate ELMs can greatly affect the fast-ion confinement [15]. In this paper, we report on the existence of an Edge Resonant Transport Layer (ERTL) responsible for the fast-ion losses observed in the presence of externally applied 3D fields. Full orbit simulations carried out with the ASCOT [16] code using the plasma response calculated with MARS-F [17] reproduce a strong correlation of the fast-ion losses with the 3D fields poloidal spectra. This work presents an analysis of fast-ion confinement in terms of the variation of the toroidal canonical momentum (δP_ϕ), which reveals resonant structures at the plasma edge activated by 3D fields that match rational orbital resonances.

This paper is structured as follows: section 2 describes the experiments carried out at AUG. In section 3, the modelling techniques using the full-orbit code ASCOT and MARS-F, which is a single fluid, full MHD eigenvalue code in full toroidal geometry, are discussed. Section 4 introduces the ERTL and describes the resonant transport mechanism that arises due to the 3D fields. In section 5, the impact of the findings

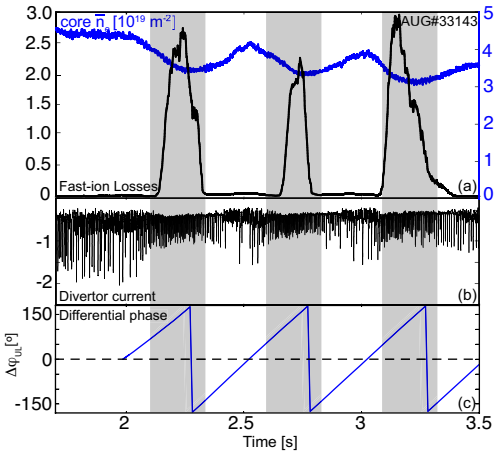

Figure 1. *AUG#33143. (a) Normalized FILD signal (black) and plasma edge electron density as functions of the applied $\Delta\varphi_{UL}$. (b) Poloidal thermo-currents from the outer divertor target plates showing ELM mitigation as a function of the applied current phase $\Delta\varphi_{UL}$ and (c) time window corresponding to the analysed $\Delta\varphi_{UL}$.*

presented with respect to fast-ion transport is assessed and a summary and conclusions are given in section 6.

2. Experiment

Several experiments have been carried out in AUG to show the impact of MPs poloidal spectra on ELM mitigation, in particular, shot #33143 with high normalized β_N, low collisionality $\nu*_e = 0.2$ and $q_{95} = 3.8$. A magnetic perturbation with a toroidal mode number $n = 2$ was generated by the ELM control coils installed in AUG, where current flowing through the lower set of coils is kept at a constant toroidal phase (ϕ_L) while the upper phase (ϕ_U) was slowly rotating at 2 Hz, introducing a phase shift ($\Delta\varphi_{UL} = \phi_U - \phi_L$) that resulted in a continuous scan in the poloidal spectra. The source of energetic particles was introduced by means of 5 MW neutral beam injection (NBI) distributed on 2 sources with 2.5 MW from 2 NBI boxes, one at 60 kV (NBI#3) the other at 93 kV (NBI#8). Figure 1 shows density pump out and partial ELM mitigation when the coils are turned on, but also a modulation with the poloidal spectra. The effect of this modulation is especially clear in the Fast Ion Lost Detector (FILD) [18] measurements, where fast-ion losses are only detected with certain coil configurations (figure 1) between $\Delta\varphi_{UL} = 120°$ and $\Delta\varphi_{UL} = 230°$.

3. Modelling

Driven by the need for an interpretation of these experimental results of fast-ion behaviour in the presence of 3D magnetic perturbations, this work analyses the effects of the MP poloidal spectra on energetic particle transport provided by a realistic modelling

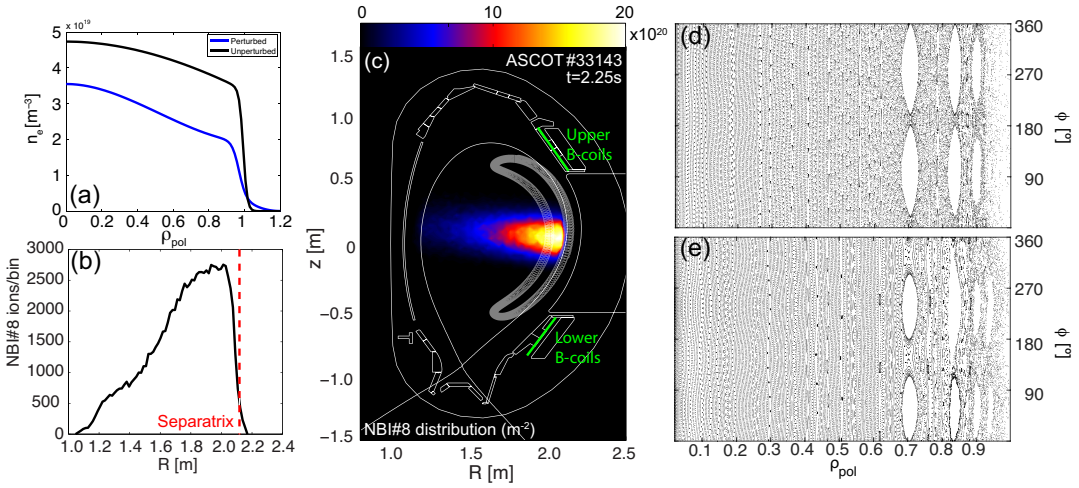

Figure 2. *AUG#33143. (a) Electron density profiles showing the unperturbed profile (black) measured at $I_{coil} = 0$ and the profile during density pump-out produced by the MP coils at $t = 2.25\,s$ (blue). (b) Birth profile distribution as a function of the plasma major radius. (c) Poloidal cross section of AUG vessel including the NBI#8 deposition using the perturbed density profile and a representative trapped orbit. Toroidal Poincaré plots showing the $n = 2$ MP perturbation for: (d) $\Delta\varphi_{UL} = 40°$, (e) $\Delta\varphi_{UL} = 260°$*

of the perturbed magnetic fields.

Modelling of these experimental measurements couples the full-orbit following code ASCOT and MARS-F code to provide reliable perturbed fields including the vacuum approach and the plasma response. The viability of this model is based on its capability of reproducing the measured data. To that end shot #33143 was used to validate the simulations. In this case, the initial fast-ion distribution was calculated for NBI#8 using the profiles at the phase where coils are turned on (figure 2(a)) as the ion deposition in the scrape-off layer (figure 2(b) and (c)) is very sensitive to density variations, entailing a significant impact on fast-ion losses. In addition, figure 4 shows the maxima of NBI#8 pitch distribution (white) and full width half maximum (grey).

The configuration of the MP coil currents was obtained for several time points and used to generate the 3D perturbation including the plasma response. Each perturbation was then added to the axisymmetric magnetic field to complete a full poloidal spectra scan. Figures 2(d) and (e) present the toroidal Poincaré plots corresponding to the configurations $\Delta\varphi_{UL} = 40°$ and $\Delta\varphi_{UL} = 260°$ calculated with MARS-F including the rotational shielding of the MP. These plots show the magnetic island structures appearing at the region $\rho_{pol} = 0.7 - 1.0$ caused by the applied perturbation. Fast-ions from NBI#8 source were followed in full orbit motion for several time windows corresponding to different poloidal spectra to reproduce the modulation of particle losses observed in FILD. To that aim, the magnetic fields including the toroidal harmonics $n = 2, 6$ were analysed to reveal the effect of each contribution. As shown in figure 3(a), all contributions led to the same tendency of total particle losses as a function of

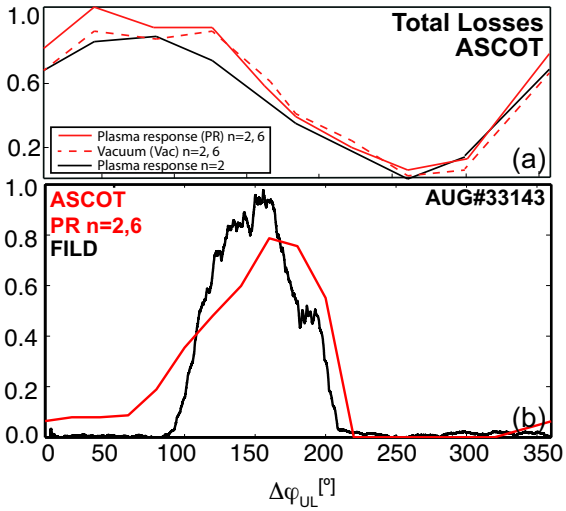

Figure 3. *(a) AUG#33143. (a) Total fast-ions losses as a function of* $\Delta\varphi_{UL}$ *including* $n = 2$ *plasma response (black),* $n = 2$ *and* $n = 6$ *plasma response (red) and* $n = 2$ *and* $n = 6$ *vacuum fields (red dashed line). (b) Normalized values of measured (black) and simulated with ASCOT (red) FILD signals as a function of the applied* $\Delta\varphi_{UL}$*.*

the poloidal spectra. These results also reveal that the impact of the plasma response on energetic particle losses changes with the poloidal MP spectra. While the plasma response and vacuum approach lead to similar fast-ion losses at $\Delta\varphi_{UL} = 260°$, the plasma response can increase the losses up to 20% at $\Delta\varphi_{UL} = 20°$.

While curves in figure 3(a) are representative of the global behaviour of NBI fast-ions under different modelling approaches, figure 3(b) show a very local behaviour, considering only lost ions reaching the FILD probe, that can be compared to the FILD measurements. In this case, the FILD signal was reproduced using the NBI#8 birth profile for all poloidal spectra including the plasma response, main toroidal harmonic $n = 2$ and $n = 6$ sidebands in our calculations. The simulation results compared to the FILD data show a good matching reproducing the behaviour of lost NBI ions reaching the FILD diagnostic, ensuring our model is capable of reproducing experimental results and can be used to make predictions for the confinement of fast-ions.

4. Edge Resonant Transport Layer (ERTL)

The experimental results show that $\Delta\phi_{UL}$ has a strong effect on fast-ion losses. Using the model described in the previous section, the phase-space of fast-ions affected by the 3D perturbation was calculated through the variation of the toroidal canonical momentum (P_ϕ) as a function of $\Delta\varphi_{UL}$. P_ϕ of a charged particle is defined as:

$$P_\phi = mRv_\phi - Ze\psi \tag{1}$$

where m is the particle mass, R is the major radius, v_ϕ is the toroidal component of the velocity, Ze is the particle charge and Ψ is the poloidal flux. P_ϕ is a constant of

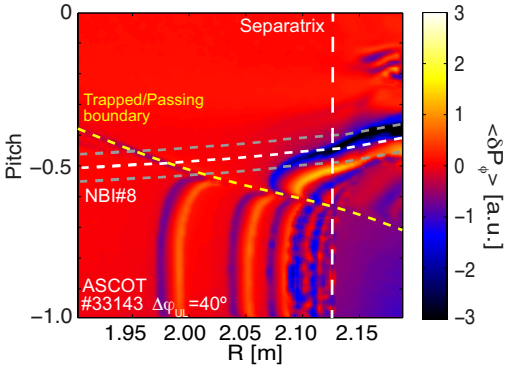

Figure 4. *AUG#33143.* $\langle \delta P_\phi \rangle$ *as a function of plasma major radius and particle pitch angle for a particle energy E=60 keV and* $z = 0$*. The fast-ion NBI#8 distribution maximum (white) and FWHM (grey). Yellow curve indicates the location of the trapped/passing boundary.*

motion for axisymmetric fields, but with the inclusion of non axisymmetric magnetic fields leading to a toroidal symmetry breaking, P_ϕ is not an invariant and its variation is associated to a radial transport of the particles. In this context, a positive variation in P_ϕ means that the particle is drifting inwards, while a negative variation leads the ion to drift outwards. The average variation of the fast-ion P_ϕ ($\langle \delta P_\phi \rangle$) was calculated as the averaged difference between the initial value of the toroidal momentum $P_\phi(0)$ and the $P_\phi(t)$ value along the particle orbit for several bouncing motions. $\langle \delta P_\phi \rangle$ is shown in figure 4 as a function of the particle pitch $\Lambda = v_\parallel / v_{tot}$ and the plasma major radius. Clear patterns appear for passing ($\Lambda \geq -0.5$ at R=2.0 m) and trapped ($\Lambda \leq -0.5$ at R=2.0 m) ions with a maximal $\langle \delta P_\phi \rangle$ located within 10 cm around the separatrix. The transport of trapped ions is dominated by resonant structures for all particle radial locations, while passing ions also show non-structured (chaotic) patterns from R=2.10 m.

$\langle \delta P_\phi \rangle$ is shown in figures 5(a)-(c) as a function of the particle energy and initial major radius with particle pitch $\Lambda = -0.5$ set by the NBI#8 injection geometry and initial z on the midplane, where $\langle \delta P_\phi \rangle$ was calculated for different coil configurations to show the impact of $\Delta\varphi_{UL}$ on energetic particle transport. In figures 5 (a)-(c), clear transport structures are observed within 5 cm around the separatrix. The maximum in simulated total losses presented in figure 3 (a) for $\Delta\varphi_{UL} = 40°$ appears correlated with a maximum outward transport as figure 5 (a) shows while the minimum in simulated total losses for $\Delta\varphi_{UL} = 260°$ appears with a maximum inward transport as figure 5 (c) shows. An intermediate configuration for $\Delta\varphi_{UL} = 160°$ leads to intermediate total losses that are reflected in a moderate transport ($\langle \delta P_\phi \rangle$) as figure 5 (b) shows.

The patterns observed in the $\langle \delta P_\phi \rangle$ plots can be understood by comparing them to the particle geometrical resonances. We use the static equilibrium for discharge AUG#33143 to calculate the particle resonances as the ratio between the bounce (ω_b) and averaged toroidal frequency ($\bar{\omega}_d$) presented in figs 5 (a)-(c). In figures 6(a) and (b) the frequency ratio has been plotted for both high and low field sides, respectively. At the low-field

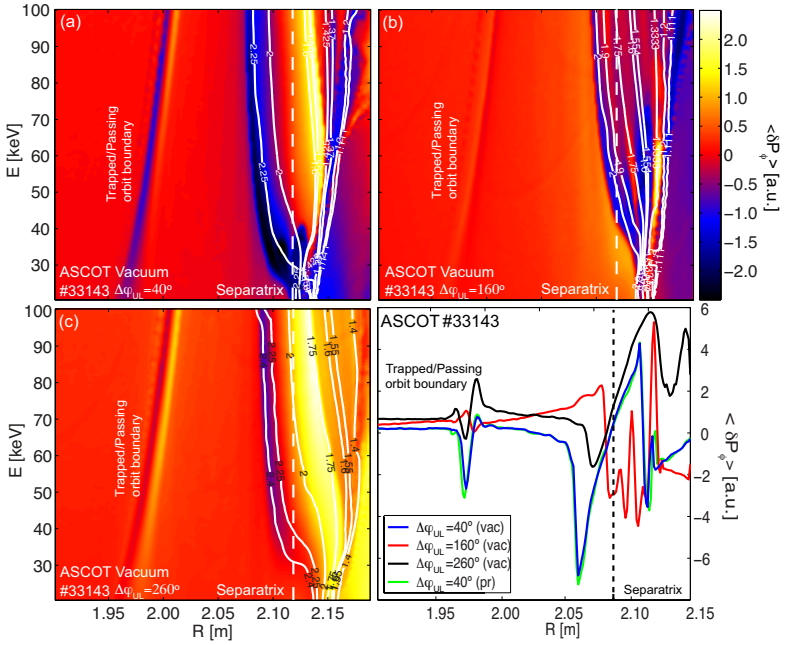

Figure 5. *AUG#33143.* $\langle \delta P_\phi \rangle$ *as a function of particle major radius and energy for: (a)*$\Delta\varphi_{UL} = 40°$*, (b)*$\Delta\varphi_{UL} = 160°$*, (c)*$\Delta\varphi_{UL} = 260°$*. White contours indicate the particle frequency ratio* $(\omega_p/\bar{\omega}_d)$*. (d) Radial profiles of* $\langle \delta P_\phi \rangle$ *for different* $\Delta\varphi_{UL}$ *at energy of E=50 keV and pitch* $\Lambda = -0.5$

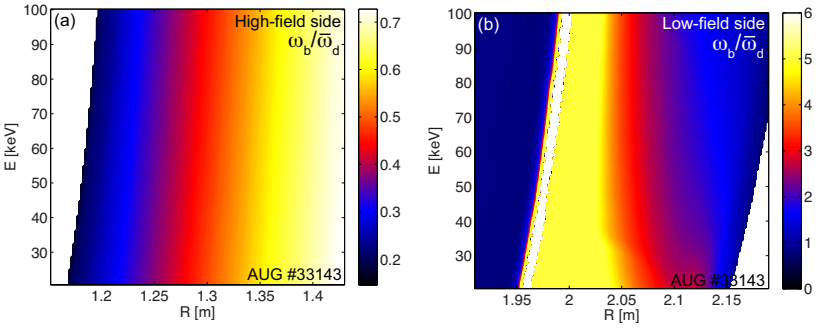

Figure 6. *AUG#33143. Energetic particle geometrical resonances as a function of energy and plasma major radius coordinates considering the average pitch of a typical NBI#8 fast-ion distribution* Λ*=-0.5 and* $z = 0$ *for (a) High-field side (HFS) and (b) Low-field side (LFS).*

side, which is mainly populated by trapped orbits, the frequency ratio exhibits a small gradient in the region close to the scrape-off layer corresponding to deeply trapped ions. This gradient increases towards the plasma core as it approaches the trapped/passing boundary, resulting in a region with very high resonance density. In the high-field side region, where the population consists of passing orbits, the geometrical resonance gradient remains almost constant and the frequency ratio has a slight dependency on the particle initial energy.

A particle resonance will be considered linear if the trajectory frequency ratio meets

the condition $n\bar{\omega}_d - p\omega_b = 0$, where p is the bounce harmonic. By overplotting the particle resonances in the $\langle \delta P_\phi \rangle$ figures of merit, a clear matching between the maxima and minima in $\langle \delta P_\phi \rangle$ and particle geometrical resonances is found. The resonances corresponding to a maximum variation of $\langle \delta P_\phi \rangle$ are $\omega_b/\bar{\omega}_d = 2.25$ for $\Delta\varphi_{UL} = 40°$, $\omega_b/\bar{\omega}_d = 2$ for $\Delta\varphi_{UL} = 160°$ and $\omega_b/\bar{\omega}_d = 1.75$ for $\Delta\varphi_{UL} = 260°$. The matching between the maxima and minima of $\langle \delta P_\phi \rangle$ and the geometrical resonances indicates that, when the perturbation is applied, the ERTL is activated by a combination of linear and nonlinear resonances, but also the area corresponding to the trapped/passing boundary presents a significant $\langle \delta P_\phi \rangle$ due to a very high density of geometrical resonances at R=1.95-2.0 m.

Most of the active resonances involved in the ERTL are nonlinear, which can be understood by considering a function describing varying field in the poloidal and toroidal direction in the form $f(r,\theta,\xi) = \sum_{n,m} e^{in\xi - im\theta} f_{m,n}(r)$ [19] in terms of particle coordinates (r,θ,ξ). The projection of the perturbation of the magnetic field along the movement of a trapped particle yields:

$$f(r,\theta,\xi) = \sum_{n,m,p\in\mathbb{Z}} e^{i(n\bar{\omega}_d + p\omega_b - \omega_0)\tau} P_{n,m,p} \cdot f_{m,n}(r,\theta,\xi) \tag{2}$$

where τ is a time variable that follows the particle location along the poloidal trajectory of period $2\pi/\omega_b$, ω_0 is the frequency of the perturbation and P is a projection operator along the orbit of the trapped particle in an axisymmetric equilibrium [19]. The linear resonant condition is met when the wave-particle phase becomes stationary, which leads to $n\bar{\omega}_d - p\omega_b = 0$ for nearly stationary magnetic perturbations ($\omega_0 = 0$). When a linear resonant condition is not satisfied, we assume that the dominant impact of the perturbation is to modulate periodically the bounce-averaged particle displacement [20]. If we consider that the periodicity of the modulation is set by the magnetic perturbation and all terms are periodic functions which can be expressed using Fourier decomposition, we can write:

$$f(r,\theta,\xi) \simeq \sum_{p,l\in\mathbb{Z}} e^{i(n\bar{\omega}_d - p\omega_b - \omega_0)\tau} e^{il(n\bar{\omega}_d - p_0\omega_b - \omega_0)\tau} P_{n,m,p} \cdot f_{m,n}(r,\theta,\xi) \tag{3}$$

for a fixed value of n, m, where l is the nonlinear harmonic, $p = p_0 + p'$ is the nonlinear bounce harmonic and p_0 the primary bounce harmonic. From eq.3, the resonant condition is given by $\frac{d}{dt}(\alpha\tau) = 0$ with $\alpha = (n\bar{\omega}_d - p\omega_b) + l(n\bar{\omega}_d - p_0\omega_b)$ for stationary perturbations and can be expressed as:

$$\frac{\omega_b}{\bar{\omega}_d} = \frac{n(1+l)}{p_0(1+l) + p'} \tag{4}$$

From expression 4 we can identify active resonances triggered by given values of $\Delta\phi_{UL}$. In the analysed shot, $n = 2$ is fixed due to the perturbation symmetry and p_0 and p' can take integer values reproducing most of the resonant structures in figures 5(a)-(c), where the amplitude and location of the activated resonance depends strongly on the frequency ratio.

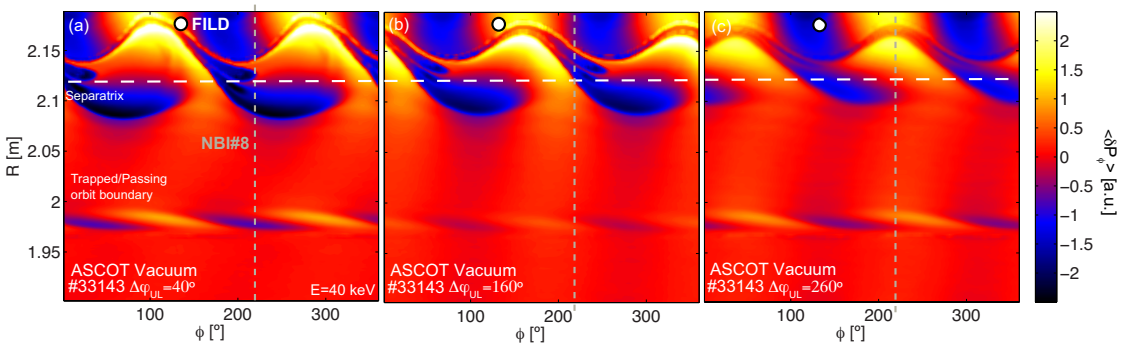

Figure 7. *AUG#33143.* $\langle \delta P_\phi \rangle$ *plot showing the LFS area as a function of plasma major radius and toroidal angle for: (a)* $\Delta\varphi_{UL} = 40°$*, (b)* $\Delta\varphi_{UL} = 160°$*,* $\Delta\varphi_{UL} = 260°$*. The location of the FILD detector is highlighted with a white circle.*

5. Main parametric dependencies of the ERTL

Using the description of the ERTL as the main transport mechanism in the presence of a 3D perturbation generated by MP coils, a complete analysis of both LFS and HFS is presented in terms of $\langle \delta P_\phi \rangle$. The role of initial toroidal phase is illustrated in figure 7. Here, $\langle \delta P_\phi \rangle$ is calculated for different $\Delta\varphi_{UL}$ indicating the NBI#8 injection. The structures in both configurations are dominated by the $n = 2$ symmetry of the applied perturbation and the activation of multiple resonances at the trapped/passing boundary. Figure 7(a) indicates that, for this configuration of $\Delta\varphi_{UL}$, the NBI injection is the least favourable with respect to the perturbation, while figure 7(b) shows the opposite.

On the magnetic HFS, the variation of $\langle \delta P_\phi \rangle$ shows a different pattern since the fast-ion population in this area consists of passing particles (figures 8 (a)-(c)). However, the variation of the poloidal spectra has a similar effect on the activated resonances, showing the maximum transport intensity at $\Delta\varphi_{UL} = 40°$ and minimum at $\Delta\varphi_{UL} = 260°$. The analysis of $\langle \delta P_\phi \rangle$ indicates that the transport is resonant in the inner plasma region, but becomes chaotic as it approaches the separatrix due to the perturbation of the magnetic field lines, which greatly passing particles.

For this case, the determination of the ratio $\omega_b/\bar{\omega}_d$ of the activated resonances was made by means of the identification of the $q = m/n$ values corresponding to the peaks in the $\langle \delta P_\phi \rangle$ radial profile at a fixed value of the energy (figures 8(d)-(f)). The calculation of $\langle \delta P_\phi \rangle$ as a function of the plasma major radius and toroidal angle (figure 9) shows a resonant structure (R=1.25-1.45 m) that is dominated by the $n = 2$ toroidal mode number of the perturbation, which corresponds to the structures observed at the associated Poincaré plots (figure 2(e) and (f)).

In addition to the $n = 2$ structures, a lobe structure is visible at the region closer to the separatrix and is most intense when the resonant magnetic configuration is applied at $\Delta\varphi_{UL} = 40°$. Note that these structures showing the fast-ion transport at the high-field side are very similar to the divertor heat flux patterns observed in the AUG

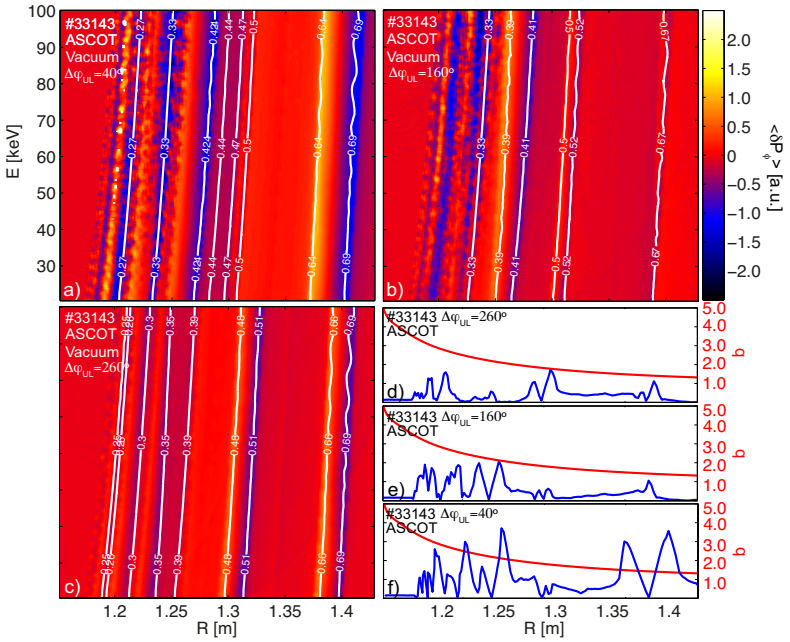

Figure 8. *AUG#33143.* $\langle \delta P_\phi \rangle$ *on the HFS area as a function of plasma major radius and energy for a fixed value of pitch* $\Lambda = -0.6$ *at: (a)*$\Delta\varphi_{UL} = 40°$*, (b)* $\Delta\varphi_{UL} = 160°$*,* $\Delta\varphi_{UL} = 260°$*. (d)-(f)* $|\ \langle \delta P_\phi \rangle\ |$ *for different* $\Delta\varphi_{UL}$ *(blue) and q-profile (red) as a function of plasma major radius.*

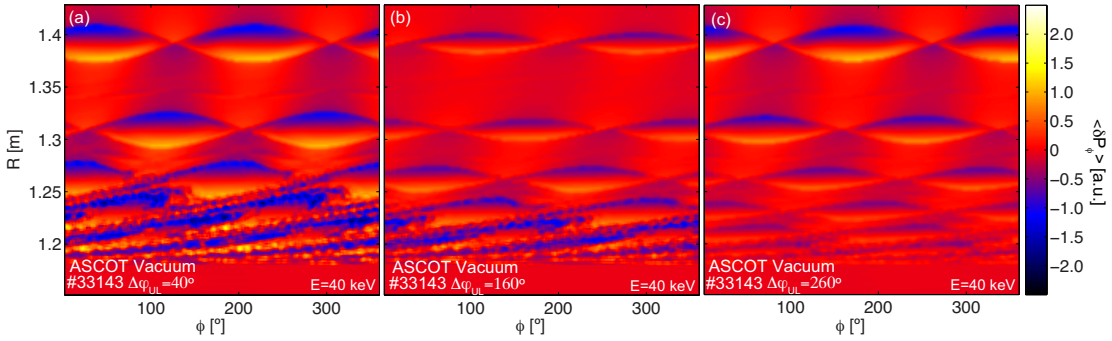

Figure 9. *Variation of* P_ϕ *on the HFS area as a function of plasma major radius and toroidal angle for: (a)* $\Delta\varphi_{UL} = 40°$*, (b)* $\Delta\varphi_{UL} = 160°$*, (c)* $\Delta\varphi_{UL} = 260°$

measurements with similar coil configurations [21].

A scan in the amplitude of the magnetic perturbation is used to analyse its effects on linear and nonlinear resonances (figures 10(a) and (b)). For amplitude levels routinely used for MP ELM suppression, both linear and nonlinear resonances are activated, but the resonant transport is mainly nonlinear (figure 10(a)). As the amplitude decreases, the intensity of nonlinear resonances ($l \neq 0$) become weaker until they completely disappear and linear resonances are the dominant transport mechanism (figure 10(b)). This fading of the $\langle \delta P_\phi \rangle$ structures is summarized in figure10(d), where structures associated to linear resonances (marked with an orange circle) are the only structures

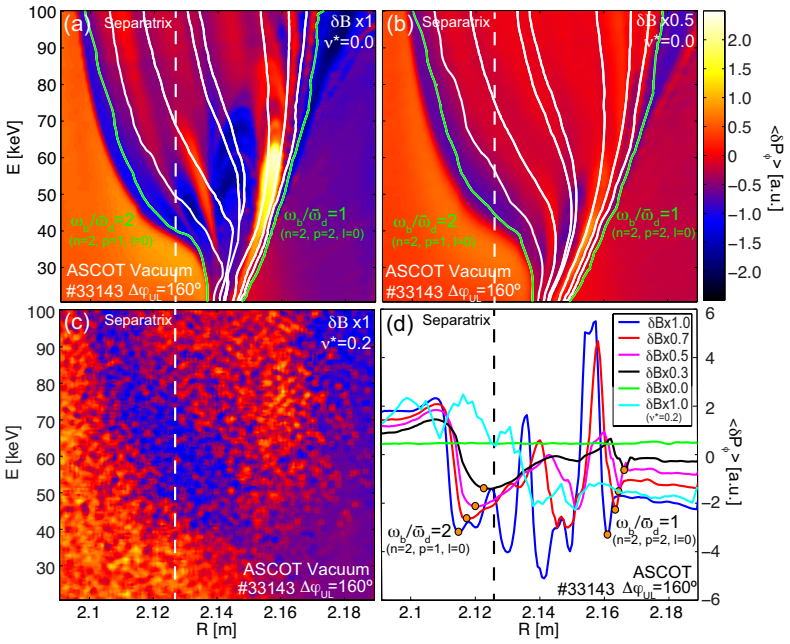

Figure 10. *AUG#33143. δP_ϕ calculated for $\Delta\varphi_{UL} = 160°$ coil configuration using 3D field amplitude of: (a) $\delta B\times 1$, (b) $\delta B\times 0.5$ and (c) $\delta B\times 1$ including collisions. Contours indicate the geometrical resonances for linear (green) and nonlinear (white) conditions. (d)$\langle\delta P_\phi\rangle$ profiles for $\Delta\varphi_{UL} = 160°$ configuration at energy E=50 keV using different δB amplitudes where linear resonances are indicated by orange circles.*

that remain when the perturbation amplitude decreases.

The impact of Coulomb collisions on the ERTL is also assessed through realistic simulations including collisions [16] between fast-ions and the bulk plasma. In figures 10(c) and (d) the impact of collisions on the ERTL leads to a widening of the resonances, but also to an overall decrease of the $\langle\delta P_\phi\rangle$ peak structure associated to the individual resonances.

The effect of the radial electric field on the ERTL was also studied. The radial electric field considered in figure11(a) was calculated for shot AUG#33143, showing the common behaviour observed in H-mode plasmas [22]. As can be observed from the comparison between figures 11(b) and 10(a), the impact of the radial electric field is to distort the resonant structures at the location of the E_r well, but it can also alter a small region outside the separatrix. This effect is related to the topology of trapped orbits (figure 2 (c)), where ions born outside the separatrix can explore more inner regions of the plasma. Although the structures are altered, the intensity of $\langle\delta P_\phi\rangle$ is not changed.

6. Summary

This work introduces an Edge Resonant Transport Layer responsible for the fast-ion losses in the presence of externally applied 3D fields in a tokamak. This transport

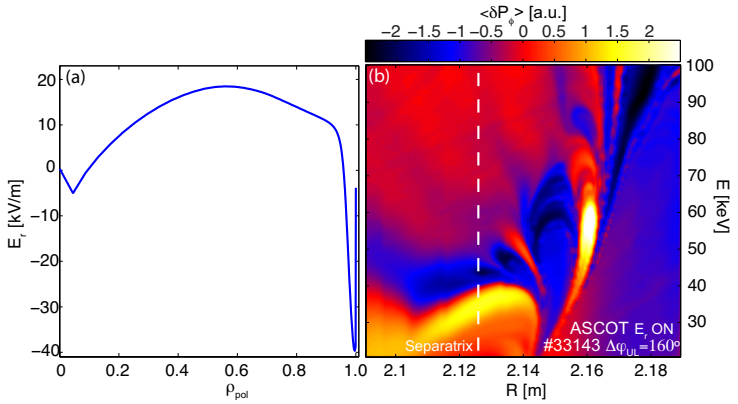

Figure 11. *AUG#33143. (a) Radial electric field profile derived from AUG experimental measurements. (b)* $\langle \delta P_\phi \rangle$ *calculated for* $\Delta\varphi_{UL} = 160°$ *coil configuration including the radial electric field.*

mechanism is shown to have a dependency on the energetic particle topology, the spatial spectrum and amplitude of the perturbation, plasma collisions and radial electric field. The dominant resonant transport is mainly linear for small amplitude perturbations, but it becomes nonlinear as the amplitude increases to levels used routinely for MP ELM suppression. When Coulomb collisions are included, the wave-particle resonant phase is lost more rapidly than in the collisionless case and, hence, the transport decreases. Also, when a radial electric field is considered, a distortion of the resonant patterns is observed near the E_r well, but the transport remains close to the separatrix and the intensity constant. The results discussed in this work were used to understand the nature of the fast-ion transport mechanism involved in the analysed experiment, but these modeling tools can also be utilized to predict the energetic particle confinement in current and future devices like ITER. Based on this, the analysis of $\langle \delta P_\phi \rangle$ can be applied to optimize future operational scenarios by modifying the ERTL, which opens the possibility of fast-ion control through the application of 3D perturbations.

Acknowledgments

This work has been carried out within the framework of the EUROfusion Consortium and has received funding from the Euratom research and training programme 2014–2018 under grant agreement number 633053. The views and opinions expressed herein do not necessarily reflect those of the European Commission. The simulations were partly performed on the MARCONI supercomputer (CINECA).

References

[1] T C Hender et al. Effect of resonant magnetic perturbations on COMPASS-C tokamak discharges. *Nucl. Fusion*, 32:2091, 1992.

[2] T E Evans et al. Suppression of Large Edge-Localized Modes in High-Confinement DIII-D Plasmas with a Stochastic Magnetic Boundary. *Phys. Rev. Lett*, 92(23):235003, 2004.

[3] Y Liang et al. Active control of type-I edge-localized modes with n=1 perturbation fields in the JET tokamak. *Phys. Rev. Lett*, 98(26):265004, 2007.

[4] W Suttrop et al. First Observation of Edge Localized Modes Mitigation with Resonant and Nonresonant Magnetic Perturbations in ASDEX Upgrade. *Phys. Rev. Lett*, 106:225004, 2011.

[5] Jong-Kyu Park. Control of Asymmetric Magnetic Perturbations in Tokamaks. *Phys. Rev. Lett*, 99(10):195003, 2007.

[6] M Willensdorfer et al. Field-Line Localized Destabilization of Ballooning Modes in Three-Dimensional Tokamaks. *Phys. Rev. Lett*, 119(8):085002, 2017.

[7] C Paz-Soldan et al. Observation of a multimode plasma response and its relationship to density pumpout and edge-localized mode suppression. *Phys. Rev. Lett*, 114(10):105001, 2015.

[8] R Nazikian et al. Pedestal Bifurcation and Resonant Field Penetration at the Threshold of Edge-Localized Mode Suppression in the DIII-D Tokamak. *Phys. Rev. Lett*, 114(5):105002, 2015.

[9] T Kurki-Suonio et al. Protecting ITER walls: fast ion power loads in 3D magnetic field. *Plasma Phys. Control. Fusion*, 59:014013, 2017.

[10] K Shinohara et al. Effects of complex symmetry-breakings on alpha particle power loads on first wall structures and equilibrium in ITER. *Nucl. Fusion*, 51:63028, 2011.

[11] K Shinohara et al. Effects of rippled fields due to ferritic inserts and ELM mitigation coils on energetic ion losses in a 15 MA inductive scenario in ITER. *Nucl. Fusion*, 52:094008, 2012.

[12] M.A. Van Zeeland et al. Fast ion transport during applied 3D magnetic perturbations on DIII-D. *Nucl. Fusion*, 55:073028, 2015.

[13] G J Kramer et al. Fast-ion effects during test blanket module simulation experiments in DIII-D Simulation of localized fast-ion heat loads in test blanket module simulation experiments on DIII-D A description of the full-particle-orbit- following SPIRAL code for simulating. *Nucl. Fusion*, 51:103029, 2011.

[14] M Garcia-Munoz et al. Fast-ion transport induced by Alfvén eigenmodes in the ASDEX Upgrade tokamak. *Nucl. Fusion*, 51:103013, 2011.

[15] M. Garcia-Munoz et al. Fast-ion losses induced by ELMs and externally applied magnetic perturbations in the ASDEX Upgrade tokamak. *Plasma Phys. Control. Fusion*, 55:124014, 2013.

[16] E Hirvijoki et al. ASCOT: Solving the kinetic equation of minority particle species in tokamak plasmas. *Comput. Phys. Commun*, 185:1310, 2014.

[17] Yueqiang Liu, M S Chu, W F Guo, and F Villone. Resistive Wall Mode Control Code Maturity. *Plasma Phys. Control. Fusion*, 52:104002, 2010.

[18] M Garcia-Munoz, H.-U Fahrbach, and H Zohm. Scintillator based detector for fast-ion losses induced by magnetohydrodynamic instabilities in the ASDEX upgrade tokamak. *Rev. Sci. Instrum.*, 80(81):053503, 2009.

[19] F Zonca, L Chen, S Briguglio, G Fogaccia, G Vlad, and X Wang. Nonlinear dynamics of phase space zonal structures and energetic particle physics in fusion plasmas. *New J. Phys.*, 17(17):013052, 2015.

[20] L. Chen and F. Zonca. Physics of Alfven waves and energetic particles in burning plasmas. *Rev. Mod. Phys.*, 88:015008, 2016.

[21] M. Faitsch, B. Sieglin, T. Eich, A. Herrmann, and W. Suttrop. 2D heat flux in ASDEX Upgrade L-Mode with magnetic perturbation. *Nuclear Materials and Energy*, 12:225004, 2017.

[22] E. Viezzer et al. High-accuracy characterization of the edge radial electric field at ASDEX Upgrade. *Nuclear Fusion*, 53(5):053005, 2013.